Molecular Doping Increases the Semi-Transparent Photovoltaic Performance of Dilute Bulk Heterojunction Film with Discontinuous Polymer Donor Networks

Yabing Tang, Hong Zheng, Xiaobo Zhou, Zheng Tang, Wei Ma, Han Yan**

Y. Tang, X. Zhou, Prof. W. Ma, Prof. H. Yan

State Key Laboratory for Mechanical Behavior of Materials

School of Materials Science and Engineering

Xi'an Jiaotong University

Xi'an 710049, P. R. China
E-mail: mseyanhan@xjtu.edu.cn

Prof. H. Zheng

Center of Nanomaterials for Renewable Energy

State Key Laboratory of Electrical Insulation and Power Equipment

School of Electrical Engineering

Xi'an Jiaotong University

Xi'an 710049, China

E-mail: zhenghong666@xjtu.edu.cn

Prof. Z. Tang

Center for Advanced Low-Dimension Materials

State Key Laboratory for Modification of Chemical Fibers and Polymer Materials

College of Materials Science and Engineering

Donghua University

Shanghai 201620, P. R. China

Keywords: organic solar cell, molecular doping, semi-transparent, dilute bulk heterojunction, non-geminate recombination

The semi-transparent and colorful properties of organic solar cells (OSCs) attract intensive academic interests due to their potential application in building integrated photovoltaics, wearable electronics, and so forth. The most straightforward and effective method to tune these optical properties is varying the componential ratio in the blend film. However, the increase in device transmittance inevitably sacrifices the photovoltaic performance because of severe carrier recombination that originates from discontinuous charge transport networks in the blend film. Herein, we propose a strategy via the molecular doping strategy to overcome these shortcomings. We discover that p-doping is able to release the trapped holes in segregated polymer domains leading to short-circuit current (J_{sc}) enhancement, while n-doping is more effective to fill the bandgap states producing a higher fill factor (*FF*). More importantly, either type of doping improves the photovoltaic performance in the semi-transparent photovoltaic devices. Our discoveries provide a new pathway to breaking the compromise between the photovoltaic performance and optical transmittance in semi-transparent OSCs, and hold promise for their future commercialization.

Broad absorption range and balanced charge transport ability are widely accepted as golden rules to make efficient solar cells. In OSCs, the active layer is made of electron-donor and acceptor networks forming nanoscale bulk heterojunction (BHJ) structure enabling efficient charge generation and undisturbed charge transport.[1,2] In contrast to the single-component active layer used in inorganic photovoltaic devices, the complementary absorption range of components in an OSC device makes it possible to tune its spectral range. It is facile to enhance the transmittance in visible light by reducing the electron-donor fraction in BHJ film while retaining higher content of fused-ring electron-acceptor that absorbs more in the infrared range. The dilute BHJ concept theoretically enhances the average visible transmittance (*AVT*) of organic blend film and makes OSC a suitable candidate for semi-transparent applications.[3-8] For practical applications in power window, a high *AVT* of 50% is necessary.[9,10] This value is roughly twice higher than that of the present in semi-transparent BHJ devices.[11-15] To achieve this goal, a strategy for power conversion efficiency (*PCE*) improvement at low donor fraction (ca. less than 20%) in dilute BHJ film needs to be developed.

Gradually reducing the electron-donor fraction arouses two morphology issues in the blend film, the discontinuous charge transport pathways and insufficient heterojunction areas for charge generation. Since efficient charge generation is the prerequisite for solar cell operation, we assume that the targeted devices with high *AVT* mainly work in the morphological region of segregated donor domains embedded in an acceptor matrix (**Figure 1**a). Under this condition, the photo-generated holes either accumulate in the segregated donor phases or transfer back to the acceptor matrix.[16] In both cases, severe non-geminate recombination takes place in the dilute BHJ film (Figure 1a). Device optimization strategies should aim both at eliminating the localized recombination centers in the donor segregations and suppressing the recombination of opposite charges in the acceptor matrix. Unfortunately, the well-established methodologies on optimizing OSCs such as molecular design and morphology modification hardly work for these geometrical defects. Alternatively, molecular doping, which introduces extra holes (p-doping) or electrons (n-doping) via electrostatic induction or certain chemical reaction, has the potential to regulate these electronic defects.[17-22] It has been reported that the *PCE* of doped OSCs was 17.1% and 17.4% in binary and ternary BHJ films after n-doping and the champion value was refreshed as 17.98% by synergistically doping the active layer and electrode interface.[23-25]

Localized charge recombination is a two-step process where holes are first trapped within the discontinuous donor phase due to the energy barrier for back transferring to the acceptor matrix and subsequently recombine with the free electrons. Our hypothesis is that the p-doping in donor pulls its highest occupied molecular orbital (HOMO) level downwards[19, 26-28] and hence reduces the localized recombination centers by making more holes transfer to the acceptor matrix (Figure 1b). On the other hand, the fluctuating potential landscape in the disordered acceptor matrix acts as “valleys” for electrons and holes.[29-31] The lack of spatial separation for opposite charges renders severe band-tail recombination in the acceptor phase.[32-33] According to Adriaenssens and Arkhipov’s recombination model in disordered semiconductor, lowering the disorder of fluctuating potential is effective to suppress the band-tail recombination.[29] Considering this occurs in the acceptor matrix, we propose that the n-doping is valid in this situation (Figure 1c).

To test the hypotheses on doping effect in the dilute BHJ film, we choose p-dopant hydrated tris(pentafluorophenyl)borane (BCF)[34-36] and n-dopant (4-(1,3-dimethyl-2,3-dihydro-1H-benzoimidazol-2-yl)phenyl)dimethylamine (N-DMBI).[37-39] The poly[(2,6-(4,8-bis(5-(2-ethylhexyl-3-fluoro)thiophen-2-yl)-benzo[1,2-b:4,5-b′]dithiophene))-alt-(5,5-(1′,3′-di-2-thienyl-5′,7′-bis(2-ethylhexyl)benzo[1′,2′-c:4′,5′-c′]dithiophene-4,8-dione)] (PM6) and 2,2′-((2Z,2′Z)-((12,13-bis(2-ethylhexyl)-3,9-diundecyl-12,13-dihydro-[1,2,5]thiadiazolo[3,4-e]thieno[2″,3″:4′,5′]thieno[2′,3′:4,5]pyrrolo[3,2-g]thieno[2′,3′:4,5]thieno[3,2-b]indole-2,10-diyl)bis(methanylylidene))bis(5,6-difluoro-3-oxo-2,3-dihydro-1H-indene-2,1-diylidene))dimalononitrile (Y6) were selected due to their complementary absorption range and high performance (**Figure 2**a).[40] The dopant-material interactions are separately examined in the solution and film absorption spectrum (Figure S1, Supporting Information). The hydrated BCF-PM6 adduct is further verified according to the polaron signals in the solution electron-spin resonance (ESR) spectra (Figure S2, Supporting Information). The transmittances of films are quantified according to the *AVT* values by considering the transparency in the visible region (370–740 nm) and the photonic response of the human eye simultaneously (see supporting information for detailed calculation method). The *AVT* of BHJ film enhances from 43.7% to 54.4% and 59.7% when the PM6 content approaches 20% and 10% in the binary blend (Figure 2b and Table S1, Supporting Information). The transmittance enhancement simultaneously brings problems of exciton splitting and charge collection in the dilute BHJ films. We evaluate the exciton splitting via measuring photoluminescence (PL) quenching efficiency, where it is expressed as $(PL_{Y6}\text{-}PL_{blend})/PL_{Y6}\times100\%$. Comparing with the BHJ film, the quenching efficiency rapidly decays until the PM6 fraction falls below 20% (Figure 2c, Figure S3, and Table S1, Supporting Information). We observe that the quenching efficiency maintains a high value of 83% even at 7% PM6 content, demonstrating the efficient exciton splitting in the high transmittance blend films. The corresponding charge collection ability is estimated by the hole mobility since the gradually reduction of PM6 content in the blend films (Figure 2c, Figure S4, and Table S1, Supporting Information). Based on the space charge limited current (SCLC) measurements, we observe a rather low plateau of hole-mobility in the range of high transmittance. The disturbed charge collection is attributed to the discontinuous PM6 phases which are evidenced by the tapping-mode atomic force microscope (TM-AFM, Figure S5, Supporting Information) and grazing incident wide-angle X-ray scattering (GIWAXS, Figure S6, Supporting Information) characterizations. Therefore, the dilute BHJ films with high transmittance mainly work under the condition with sufficient charge generation and insufficient charge collection. We take the PM6 fraction of 7% with minimum hole mobility as the testbed for further doping studies. At this point, the color coordinate shifts from a blue point (0.2865, 0.2952) of BHJ film to (0.3029, 0.3173) (Figure S7 and Table S1, Supporting Information), which is close to the "white point" D65 (0.3128, 0.3290) for application in power windows.

We next fabricated photovoltaic devices of PM6:Y6 (0.07:1) to test whether the molecular doping leads to improved device performance. Comparing with the standard BHJ device, the device with a PM6:Y6 ratio of 0.07:1 sacrifices its J_{sc} and *FF* (Figure S8 and Table S2, Supporting Information). With appropriate content of dopants in the 0.07:1 blend film, we find that either type of doping enhances the photovoltaic performance (Figure 2d, **Table 1**, and Table S3, Supporting Information). For the p-doped devices, the *PCE* enhancement is mainly ascribed to the improved J_{sc}, where it increases from 17.1±0.2 mA cm^{-2} to 18.1±0.3 mA cm^{-2}. While n-doping barely changes the J_{sc}, the *PCE* enhancement stems from the combined improvement in both of the open-circuit voltage (V_{oc}) and *FF*. The J_{sc} variation is further confirmed by the external quantum efficiency (*EQE*) measurements, which give consistent current densities of 17.2, 18.1, and 17.3 mA cm^{-2} in the control, p-doped, and n-doped devices respectively (Figure 2e). The photocurrents (J_{ph}) enhancement upon p-doping falls off along with the increased effective voltage (V_{eff}) (Figure 2f). Biasing the V_{eff} at 3 V, J_{ph} of the p- and n-doped devices saturates to the same value with the un-doped counterpart. These results demonstrate that doping by either polarity does not change the absorbed photon numbers in the dilute BHJ film. P-doping is equivalent to the increase of built-in potential which facilitates the free charge generation. In contrast, n-doping only functions in the working region of the cell (moderate V_{eff}, from 0.10 to 0.80 V), which is consistent with the common sense of reduced charge recombination in the blend film. We emphasize that the J_{sc} contribution from the self-dissociation of Y6 excitons only accounts for a small part, due to the low J_{sc} of 0.26 mA cm^{-2} in the single-component Y6 device. In addition, n-doping doesn't improve this process with invariant J_{sc} value (Figure S9 and Table S4, Supporting Information). Additional proofs from morphology characterizations reveal that neither of p-doping nor n-doping alters the dilute BHJ morphology to optimize the device performance (Figure S10 and S11, Table S5, Supporting Information). Therefore the optimized photovoltaic performances solely come from the electronic modification by molecular doping.

According to our proposed doping benefits on photovoltaic performance in the dilute BHJ film (Figure 1), p-doping increases the number of photo-generated free carriers by de-trapping the holes from segregated PM6 domains, whereas n-doping suppresses the recombination between free carriers and trapped carriers due to the energy landscape fluctuation within continuous Y6 phases. We run density functional theory (DFT) calculation to predict the roles of hydrated BCF addition on the energy level shift of PM6 (**Figure 3**a and Figure S12, Supporting Information). The computational details are provided in the Supporting Information. In the hydrated BCF, the oxygen atom of water molecule is chemically adsorbed by the boron atom of the BCF molecule (Figure S12, Supporting Information). On the other hand, the hydrogen atom of water molecule can be adsorbed by one of the carbonyl groups of PM6 with a moderate O-H distance of 1.469 Å (Figure 3a), indicating a typical hydrogen bond between the hydrated BCF and PM6. The natural bond orbital (NBO) analyses reveal partial charge transfer (0.58 e) from PM6 to hydrated BCF, indicating orbital overlap between the HOMO of PM6 and the lowest unoccupied molecular orbital (LUMO) of hydrated BCF. Such chemical adsorption induces mild downcome of HOMO/LUMO levels of PM6. As displayed in Figure 3b, the adsorption of hydrated BCF on PM6 pulls down the PM6 HOMO level by 0.12 eV. Simultaneously, neither of hydrated BCF nor hybridized complex introduces new hole trap sites within PM6 bandgap (Figure 3b). The reduced energy barrier for hole-transfer from PM6 to Y6 helps literate the localized holes, which re-contributes to the J_{sc} by increasing the free carrier density in Y6. The distribution of energy landscapes in organic semiconductors is depicted by Gaussian disorder model (GDM).[41-42] It deciphers the thermally assisted tunneling process between neighboring transport sites, and correlates the mobility with temperature and disorder.[43] At low doping concentration, the small amount of counterions does not contribute to either structural (Figure S10 and S11, Supporting Information) or energetic disorder, therefore the total Gaussian disorder should be reduced accompanying with the doping-filled band-tail.[44-45] Due to the inferior electron transport property of Y6 (Figure S13 and Table S1, Supporting Information), we focus on its electron transporting energetic disorder (σ). It is calculated according to Equation (1)

$$\mu_0 = \mu_\infty exp\left[-\frac{4}{9}\left(\frac{\sigma}{k_B T}\right)^2\right] \tag{1}$$

where μ_0 is the zero-field mobility, μ_∞ is the upper limit of the mobility, T is the temperature, and k_B represents for the Boltzmann constant. The Gaussian disorder decreases from 26.1 meV to 16.0 meV and 13.9 meV via p- and n-doping respectively (Figure 3c, Figure S14, Supporting Information). We deduce that p-doping reduces σ due to the decreased electron trap density in segregated PM6 domains. Lower σ values release the trapped carriers in the band-tail, and hence improve the photovoltaic performance for better charge transport in the dilute BHJ film. The above analysis well explains the J_{sc} enhancement via p-doping, and points out that either doping polarity suppresses the non-geminate recombination in the dilute BHJ film which might be the origin of better FF and V_{oc}.

The FF in OSC has been well-related to Figure of Merits (FoM) θ and α.[46-48] Bartesaghi et al. proposed the parameter θ as a measure of the ratio of the recombination to extraction rates,

$$\theta = \frac{k_{rec}}{k_{ext}} = \frac{\gamma G d^4}{\mu_n \mu_p V_{int}^2} \tag{2}$$

where k_{rec} and k_{ext} are the recombination and extraction rates, γ is the bimolecular recombination coefficient, G is the charge generation rate, d is the film thickness, μ_n and μ_p are the electron and hole mobilities, and V_{int} is the internal voltage. The measurements of γ, G, μ_n and, μ_p are described in the supporting information,[49] and the corresponding results are displayed in Figure S15 and Table S6

(Supporting Information). In Figure 3d, we observe that θ reduces from 4.5×10^{-3} to 3.4×10^{-3} and 2.9×10^{-3} upon p- and n-doping. The lower θ values are consistent with the *FF* enhancements.[47] The parameter θ can be related to the drift length (l_{dr}) of carriers driven by the V_{int} under short-circuit condition, which is expressed by $\theta=d^2/l_{dr}^2$.[46] The l_{dr} of the un-doped film is 1.27×10^3 nm, which is much higher than the film thickness of 85 nm (Figure 3d). Though either types of doping increase the l_{dr}, the larger l_{dr} from smaller σ in the n-doped Y6 is more beneficial for the *FF* improvement. In the transport-limited device, Neher et al. proposed another parameter α to analytically depict the balance between the free charge recombination and extraction,

$$\alpha = \sqrt{\frac{q^2\gamma G d^4}{4\mu_n\mu_p(k_BT)^2}} \tag{3}$$

where q is the elemental charge. The parameter α decreases from 1.08 of un-doped sample to below 1 after doping, demonstrating reduced charge transport loss (Figure 3e).[48] Based on α, we are able to calculate the diffusion length (l_{dif}) according to $\alpha=d^2/2l_{dif}^2$.[46] The l_{dif} enhances from 58 nm to 65 nm and 67 nm respectively via p- and n-doping (Figure 3e). Both of the increased l_{dr} and l_{dif} undoubtedly point out that either type of doping increases the *FF* via enhanced charge transport, and n-doping is more efficient for it decreasing the energetic disorder most. The charge transport is often evaluated by the product of carrier mobility and lifetime. Since n-doping slightly decreases the carrier mobility in the dilute blend film (Figure S15b and c, and Table S6, Supporting Information), the longer carrier lifetime according to the transient photovoltage (TPV) measurements is key to the enhanced *FF* in our experiments (Figure 3f).

In order to understand the doping effect on V_{oc}, we studied the energy loss with combined characterizations of photovoltaic *EQE* (Figure S16, Supporting Information) and electroluminescence *EQE* (EQE_{EL}, Figure 3g).[50-52] We observe that neither type of doping changes the photovoltaic bandgap (E_g^{PV}, see more details in the supporting information). Though the E_g^{PV} of 1.367 eV in the dilute BHJ film is lower than that of 1.382 eV in the BHJ film, the charge-transfer (*CT*) states are constant at ~1.310 eV (Figure S17 and Table S7, Supporting Information). The constant *CT* position demonstrates that exciton splitting in the dilute BHJ devices obeys the same principle with the BHJ devices, and the V_{oc} variation comes from the carrier recombination due to the discontinuous morphology. After evaluating the three parts of energy loss in OSC (see supporting information), we conclude that the V_{oc} enhancement after n-doping is due to the reduction in the non-radiative loss from 0.220 eV to 0.185 eV (Figure 3h). Its reduction can be related to the doping-filled band-tail states,[53] which will be thoroughly discussed in our following work.

Since we have fully demonstrated that adding either type of dopants can enhance the photovoltaic performance of the dilute BHJ film, we now explore its potential in semi-transparent photovoltaic devices. The semi-transparent devices were fabricated by replacing the topmost 100 nm-thick Al cathode with a laminated cathode of 9 nm-thick Ag onto a 2 nm-thick Al seed layer. The *AVT* values of the semi-transparent devices vary between the range of BHJ to pure Y6 film, namely between 20.9% to 41.4% (**Figure 4**a and Table S8, Supporting Information). The relatively low *AVT* values are limited by the transmittance of the top cathode. The color coordinate correspondingly shifts from a blue point (0.2576, 0.2755) of BHJ film to white point (0.3002, 0.3165) of pure Y6 film (Figure 4b and Table S8, Supporting Information), which is visualized by the photographs taken through the devices (Figure 4c). We first measure the device with PM6:Y6 ratio of 0.07:1, which is the research object in our mechanism study. P-doping increases J_{sc} from 9.3±0.3 mA cm^{-2} to 10.6±0.2 mA cm^{-2}, while n-doping leads to a large *FF* enhancement from 52.4% to 59.9% (Figure 4d and **Table 2**). The J_{sc} variation is consistent with the *EQE* measurements, where the integrated current density demonstrates an improvement of 1.3 mA cm^{-2} after p-doping (Figure 4f). Compared to the BHJ device, though the dilute BHJ device exhibits a much higher *AVT* value of 38.1%, their low *PCE* of only 4.1% limits their application in semi-transparent photovoltaics. In order to obtain higher *PCE* values, we appropriately increase the PM6 content to 20%. It is impressive that *PCE* enhancement after doping is visible even when the PM6 content reaches 15% (Figure S18, Table 2 and Table S9, Supporting Information), where the J_{sc} is increased from 14.2±0.2 mA cm^{-2} to 14.6±0.3 mA cm^{-2} after p-doping and *FF* is enhanced from 62.3% to 65.3% after n-doping (Figure 4e). The increased J_{sc} is well supported by the *EQE* measurements from 13.8 mA cm^{-2} to 14.6 mA cm^{-2} (Figure 4g). To fairly compare the properties of semi-transparent devices with variation in both *AVT* and *PCE*, we adopted another figure of merit light utilization efficiency (*LUE* = *AVT* × *PCE*). When the PM6 content reaches 15%, it exhibits an *LUE* value of 2.61% without doping, which is comparable to the BHJ devices of 2.55% (Figure S18a and b, and Table S9, Supporting Information). Under this condition, p-doping increases the *LUE* value to 2.80%, which is higher than that of the BHJ device.

In summary, we study the effects of either p- or n-type molecular doping on the photovoltaic performance of dilute PM6:Y6 BHJ film with low donor content. We find that adding p-dopants enables the trapped holes to transfer from the segregated PM6 domains back to the continuous Y6 phase leading to enhanced J_{sc}. While n-doping fills the band-tail states of Y6 phase resulting in better *FF* and V_{oc}. We further apply the molecular doping in semi-transparent dilute BHJ devices, displaying superior *LUE* values as compared to the widely used BHJ films. As adjusting donor:acceptor ratio is the most effective strategy in developing colorful and semi-transparent OSC and the inevitable geometry defects are unlike to be solved by other means exemplified by molecular design and morphology modification, we envisage that our discovery opens new avenues for future application of OSC based power window. Further studies on novel transparent electrodes, and organic photovoltaic materials screening, will lead to future progress in molecularly doped semi-transparent OSCs.

Supporting Information

Supporting Information is available from the Wiley Online Library or from the author.

Acknowledgements

Thanks for the support from the National Natural Science Foundation of China (21975198 and 51803162), the Key Scientific and Technological Innovation Team Project of Shaanxi Province (2020TD-002), the Natural Science Basic Research Program of Shaanxi (2021JM-005), and 111 project 2.0 (BP2018008).

X-ray data of the control and doped films with various PM6:Y6 weight ratios (1:0, 0:1, 0.01:1, 0.07:1) was acquired at beamlines 7.3.3 at the Advanced Light Source, which is supported by the Director, Office of Science, Office of Basic Energy Sciences, of the U.S. Department of Energy under Contract No. DE-AC02-05CH11231. The authors thank Chenhui Zhu at beamline 7.3.3 for assistance with data acquisition. The X-ray data of PM6:Y6 (0.20:1) and BHJ film was undertaken on the SAXS/WAXS beamline at the Australian Synchrotron, part of ANSTO. The authors thank Dr. Nigel Kirby and Dr. Susanne Seibt for assistance with data acquisition.

We thank Miss Hang Guo at Instrument Analysis Center of Xi'an Jiaotong University for her assistance with PL measurement.

Conflict of Interest

The authors declare no conflict of interest.

Received: ((will be filled in by the editorial staff))
Revised: ((will be filled in by the editorial staff))
Published online: ((will be filled in by the editorial staff))

References

[1] G. Yu, J. Gao, J. C. Hummelen, F. Wudl, A. J. Heeger, *Science* **1995**, *270*, 1789.

[2] J. J. M. Halls, C. A. Walsh, N. C. Greenham, E. A. Marseglia, R. H. Friend, S. C. Moratti, A. B. Holmes, *Nature* **1995**, *376*, 498.

[3] Z. Hu, Z. Wang, F. Zhang, *J. Mater. Chem. A* **2019**, *7*, 7025.

[4] Y. Xie, Y. Cai, L. Zhu, R. Xia, L. Ye, X. Feng, H. L. Yip, F. Liu, G. Lu, S. Tan, and Y. Sun, *Adv. Funct. Mater.* **2020**, *30*, 2002181.

[5] L. Zuo, X. Shi, W. Fu, A. K.-Y. Jen, *Adv. Mater.* **2019**, *31*, 1901683.

[6] Z. Hu, J. Wang, X. Ma, J. Gao, C. Xu, X. Wang, X. Zhang, Z. Wang, F. Zhang, *J. Mater. Chem. A*, **2021**, *9*, 6797.

[7] P. Cheng, H. Wang, Y. Zhu, R. Zheng, T. Li, C. Chen, T. Huang, Y. Zhao, R. Wang, D. Meng, Y. Li, C. Zhu, K. Wei, X. Zhan, Y. Yang, *Adv. Mater.* **2020**, *32*, 2003891.

[8] C. Xu, K. Jin, Z. Xiao, Z. Zhao, X. Ma, X. Wang, J. Li, W. Xu, S. Zhang, L. Ding, F. Zhang, *Adv. Funct. Mater.* **2021**, 2107934.

[9] C. J. Traverse, R. Pandey, M. C. Barr, R. R. Lunt, *Nat. Energy* **2017**, *2*, 849.

[10] I. Burgue's-Ceballos, L. Lucera, P. Tiwana, K. Ocytko, L. Tan, S. Kowalski, J. Snow, A. Pron, H. Bürckstümmer, N. Blouin, G. Morse, *Joule* **2021**, *5*, 2261.

[11] Y. Bai, C. Zhao, X. Chen, S. Zhang, S. Zhang, T. Hayat, A. Alsaedi, Z. Tan, J. Hou, Y. Li, *J. Mater. Chem. A* **2019**, *7*, 15887.

[12] D. Wang, R. Qin, G. Zhou, X. Li, R. Xia, Y. Li, L. Zhan, H. Zhu, X. Lu, H. L. Yip, H. Chen, C. Li, *Adv. Mater.* **2020**, *32*, 2001621.

[13] W. Song, B. Fanady, R. Peng, L. Hong, L. Wu, W. Zhang, T. Yan, T. Wu, S. Chen, Z. Ge, *Adv. Energy Mater.* **2020**, *10*, 2000136.

[14] X. Lu, L. Cao, X. Du, H. Lin, C. Zheng, Z. Chen, B. Sun, S. Tao, *Adv. Optical Mater.* **2021**, *9*, 2100064.

[15] Y. Song, K. Zhang, SDong, R. Xia, F. Huang, Y. Cao, *ACS Appl. Mater. Interfaces* **2020**, *12*, 18473.

[16] G. Zhang, X. Chen, J. Xiao, P. C. Y. Chow, M. Ren, G. Kupgan, X. Jiao, C. C. S. Chan, X. Du, R. Xia, Z. Chen, J. Yuan, Y. Zhang, S. Zhang, Y. Liu, Y. Zou, H. Yan, K. S. Wong, V. Coropceanu, N. Li, C. J. Brabec, J.-L. Bredas, H.-L. Yip, Y. Cao, *Nat. Commun.* **2020**, *11*, 3943.

[17] H. Yan, J. G. Manion, M. Yuan, F. P. Garcia de Arquer, G. R. McKeown, S. Beaupre, M. Leclerc, E. H. Sargent, D. S. Seferos, *Adv. Mater.* **2016**, *28*, 6491.

[18] H. Yan, J. Chen, K. Zhou, Y. Tang, X. Meng, X. Xu, W. Ma, *Adv. Energy Mater.* **2018**, *8*, 1703672.

[19] H. Yan, Y. Tang, X. Sui, Y. Liu, B. Gao, X. Liu, S. F. Liu, J. Hou, W. Ma, *ACS Energy Lett.* **2019**, *4*, 1356.

[20] Y. Tang, B. Lin, H. Zhao, T. Li, W. Ma, H. Yan, *ACS Appl. Mater. Interfaces* **2020**, *12*, 13021.

[21] W. Xue, Y. Tang, X. Zhou, Z. Tang, H. Zhao, T. Li, L. Zhang, S. Liu, C. Zhao, W. Ma, H. Yan, *Adv. Funct. Mater.* **2021**, *31*, 2101892.

[22] H. Yan, W. Ma, Adv. Funct. Mater. 2021, 31, 2111351.

[23] Y. Lin, M. I. Nugraha, Y. Firdaus, A. D. Scaccabarozzi, F. Aniés, A.-H. Emwas, E. Yengel, X. Zheng, J. Liu, W. Wahyudi, E. Yarali, H. Faber, O. M. Bakr, L. Tsetseris, M. Heeney, T. D. Anthopoulos, *ACS Energy Lett.* **2020**, *5*, 3663.

[24] Y. Lin, Y. Firdaus, M. I. Nugraha, F. Liu, S. Karuthedath, A.-H. Emwas, W. Zhang, A. Seitkhan, M. Neophytou, H. Faber, E. Yengel, I. McCulloch, L. Tsetseris, F. Laquai, T. D. Anthopoulos, *Adv. Sci.* **2020**, *7*, 1903419.

[25] Y. Wang, Y. Zhang, T. Shan, Q. Wei, Z. Xu, Y. Zhao, J. Yang, Q. Bao, H. Jin, Z. Ma, H. Wei, H. Zhong, *J. Mater. Chem. A* **2021**, *9*, 25629.

[26] I. Salzmann, G. Heimel, M. Oehzelt, S. Winkler, N. Koch, *Acc. Chem. Res*. **2016**, *49*, 370.

[27] B. Wegner, D. Lungwitz, A. E. Mansour, C. E. Tait, N. Tanaka, T. Zhai, S. Duhm, M. Forster, J. Behrends, Y. Shoji, A. Opitz, U. Scherf, E. J. W. List-Kratochvil, T. Fukushima, N. Koch, *Adv. Sci*. **2020**, *7*, 2001322.

[28] Z. Liang, H. H. Choi, X. Luo, T. Liu, A. Abtahi, U. S. Ramasamy, J. A. Hitron, K. N. Baustert, J. L. Hempel, A. M. Boehm, A. Ansary, D. R. Strachan, J. Mei, C. Risko, V. Podzorov, K. R. Graham, *Nat. Mater*. **2021**, *20*, 518.

[29] G. J. Adriaenssens, V. I. Arkhipov, *Solid State Commun.* **1997**, *103*, 541.

[30] G. Lakhwani, A. Rao, R. H. Friend, *Annu. Rev. Phys. Chem.* **2014**, *65*, 557.

[31] A. Wagenpfahl, *J. Phys.: Condens. Matter* **2017**, *29*, 373001.

[32] B. Xiao, P. Calado, R. C. I. MacKenzie, T. Kirchartz, J. Yan, J. Nelson, *Phys. Rev. Appl*. **2020**, *14*, 024034.

[33] T. Kirchartz, J. Nelson, *Phys. Rev. B* **2012**, *86*, 165201.

[34] B. Yurash, D. X. Cao, V. V. Brus, D. Leifert, M. Wang, A. Dixon, M. Seifrid, A. E. Mansour, D. Lungwitz, T. Liu, P. J. Santiago, K. R. Graham, N. Koch, G. C. Bazan, T.-Q. Nguyen, *Nat. Mater.* **2019**, *18*, 1327.

[35] E. H. Suh, J. G. Oh, J. Jung, S. H. Noh, T. S. Lee, J. Jang, *Adv. Energy Mater*. **2020**, *10*, 2002521.

[36] H. Yan, W. Ma, *Nat. Mater.* **2019**, *18*, 1269.

[37] P. Wei, J. H. Oh, G. Dong, Z. Bao, *J. Am. Chem. Soc.* **2010**, *132*, 8852.

[38] P. Wei, T. Menke, B. D. Naab, K. Leo, M. Riede, Z. Bao, *J. Am. Chem. Soc.* **2012**, *134*, 3999.

[39] B. D. Naab, S. Himmelberger, Y. Diao, K. Vandewal, P. Wei, B. Lussem, A. Salleo, Z. Bao, *Adv. Mater*. **2013**, *25*, 4663.

[40] J. Yuan, Y. Zhang, L. Zhou, G. Zhang, H. L. Yip, T. K. Lau, X. Lu, C. Zhu, H. Peng, P. A. Johnson, M. Leclerc, Y. Cao, J. Ulanski, Y. Li, Y. Zou, *Joule* **2019**, *3*, 1140.

[41]L. Pautmeier, R. Richert, H. Bässler, *Synth. Met.* **1990**, *37*, 271.

[42] W. F. Pasveer, J. Cottaar, C. Tanase, R. Coehoorn, P. A. Bobbert, P. W. M. Blom, D. M. de Leeuw, M. A. J. Michels, *Phys. Rev. Lett.* **2005**, *94*, 206601.

[43] J. Cottaar, L. J. A. Koster, R. Coehoorn, P. A. Bobbert, *Phys. Rev. Lett.* **2011**, *107*, 136601.

[44] V. I. Arkhipov, P. Heremans, E. V. Emelianova, G. J. Adriaenssens, H. Bässler, *J. Non-Cryst. Solids* **2004**, *338*, 603.

[45] S. Olthof, S. Mehraeen, S. K. Mohapatra, S. Barlow, V. Coropceanu, J.-L. Bre´das, S. R. Marder, A. Kahn, *Phys. Rev. Lett.* **2012**, *109*, 176601.

[46] N. Tokmoldin, J. Vollbrecht, S. M. Hosseini, B. Sun, L. Perdigón-Toro, H. Y. Woo, Y. Zou, D. Neher, S. Shoaee, *Adv. Energy Mater*. **2021**, 2100804.

[47] D. Bartesaghi, I. d. C. Pérez, J. Kniepert, S. Roland, M. Turbiez, D. Neher, L. J. A. Koster, *Nat. Commun.* **2015**, *6*, 7083.

[48] D. Neher, J. Kniepert, A. Elimelech, L. J. Koster, *Sci. Rep.* **2016**, *6*, 24861.

[49] L. J. A. Koster, M. Kemerink, M. M. Wienk, K. Maturová, R. A. J. Janssen, *Adv. Mater,* **2011**, *23*, 1670.

[50] U. Raua, J. H. Werner, *Appl. Phys. Lett.* **2004**, *84*, 3735.

[51] Rau. U, *Phys. Rev. B* **2017**, *76*, 085303.

[52] J. Liu, S. Chen, D. Qian, B. Gautam, G. Yang, J. Zhao, J. Bergqvist, F. Zhang, W. Ma, H. Ade, O. Inganäs, K. Gundogdu, F. Gao, H. Yan, *Nat. Energy* **2016**, *1*, 16089.

[53] S. Liu, J. Yuan, W. Deng, M. Luo, Y. Xie, Q. Liang, Y. Zou, Z. He, H. Wu, Y. Cao, *Nat. Photonics* **2020**, *14*, 300.

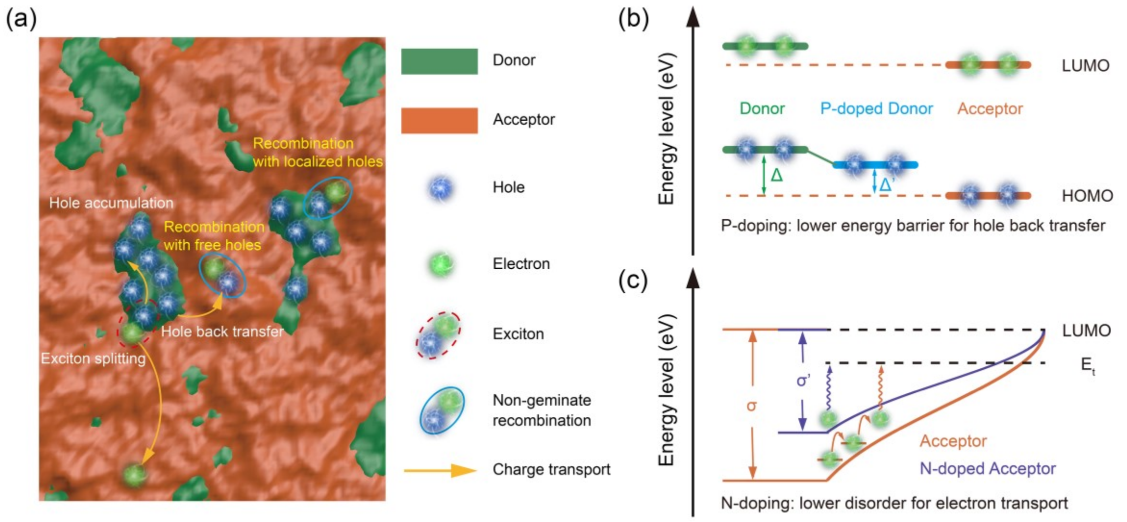

Figure 1. (a) Scheme of the non-geminate recombination pathways in the dilute BHJ film: electrons recombinating with the localized holes in donor segregations and with the holes in acceptor. (b) Mechanism scheme of p-doping on suppressed non-geminate recombination in dilute BHJ film. (c) Mechanism scheme of the n-doping on suppressed non-geminate recombination in dilute BHJ film.

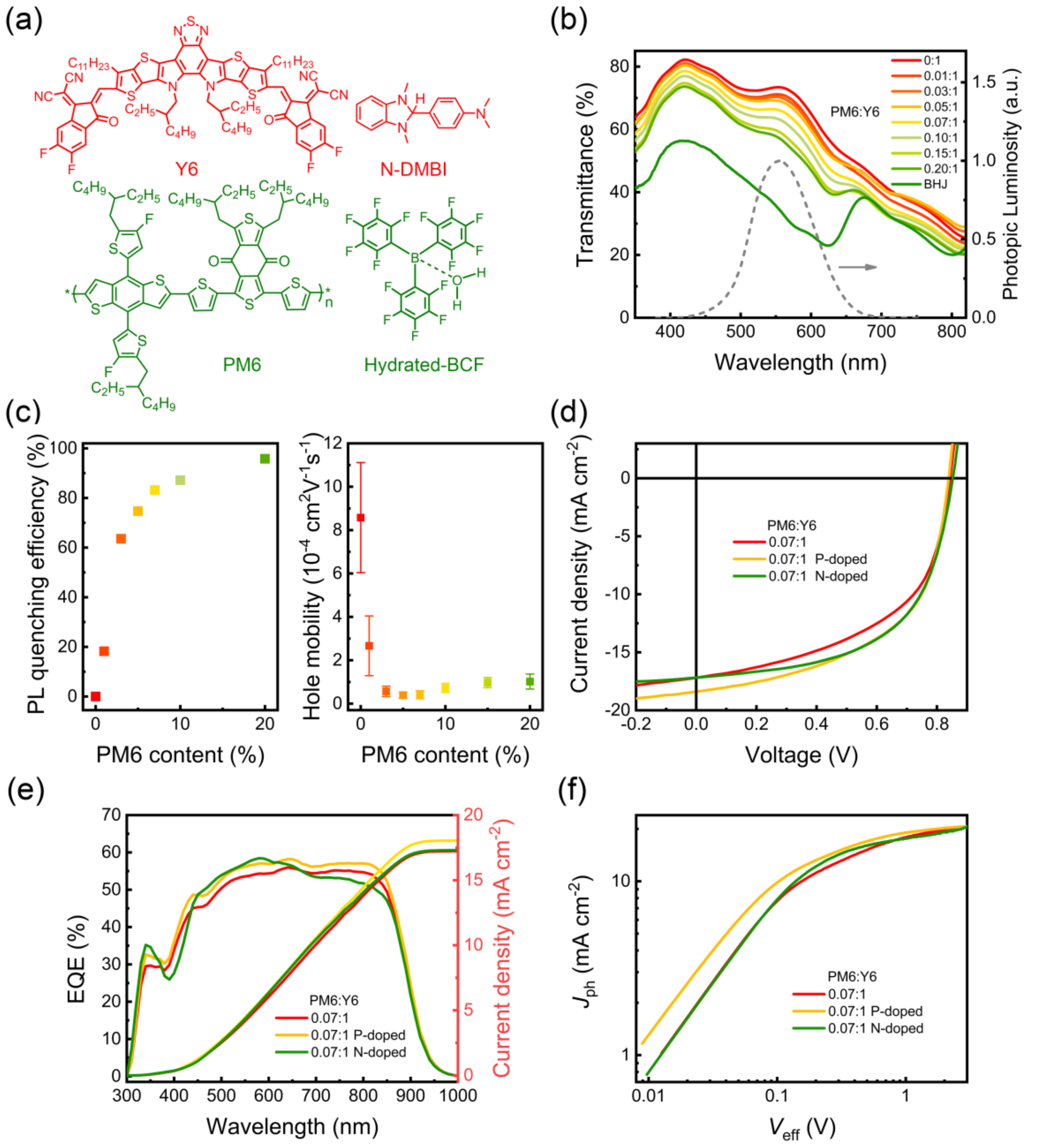

Figure 2. (a) The chemical structures of PM6, Y6, hydrated BCF, and N-DMBI. (b) The transmittance spectra of blend films with various PM6:Y6 weight ratios (0:1, 0.01:1, 0.03:1, 0.05:1, 0.07:1, 0.10:1, 0.15:1, 0.20:1, 0.83:1) and the photonic response of the human eye. (c) The PL quenching efficiency of PM6:Y6 films with various weight ratios (0:1, 0.01:1, 0.03:1, 0.05:1, 0.07:1, 0.10:1, 0.20:1) and the statistical hole mobility of hole-only devices with various PM6:Y6 weight ratios (0:1, 0.01:1, 0.03:1, 0.05:1, 0.07:1, 0.10:1, 0.15:1, 0.20:1). (d) The *J-V* curves of the control, 0.5 wt% hydrated BCF, and 0.1 wt% N-DMBI doped opaque PM6:Y6 (0.07:1) devices. (e) *EQE* and

corresponding integrated current density curves of the control, 0.5 wt% hydrated BCF doped, and 0.1 wt% N-DMBI doped opaque PM6:Y6 (0.07:1) devices. (f) J_{ph}–V_{eff} curves for the control, 0.5 wt% hydrated BCF doped, and 0.1 wt% N-DMBI doped PM6:Y6 (0.07:1) films.

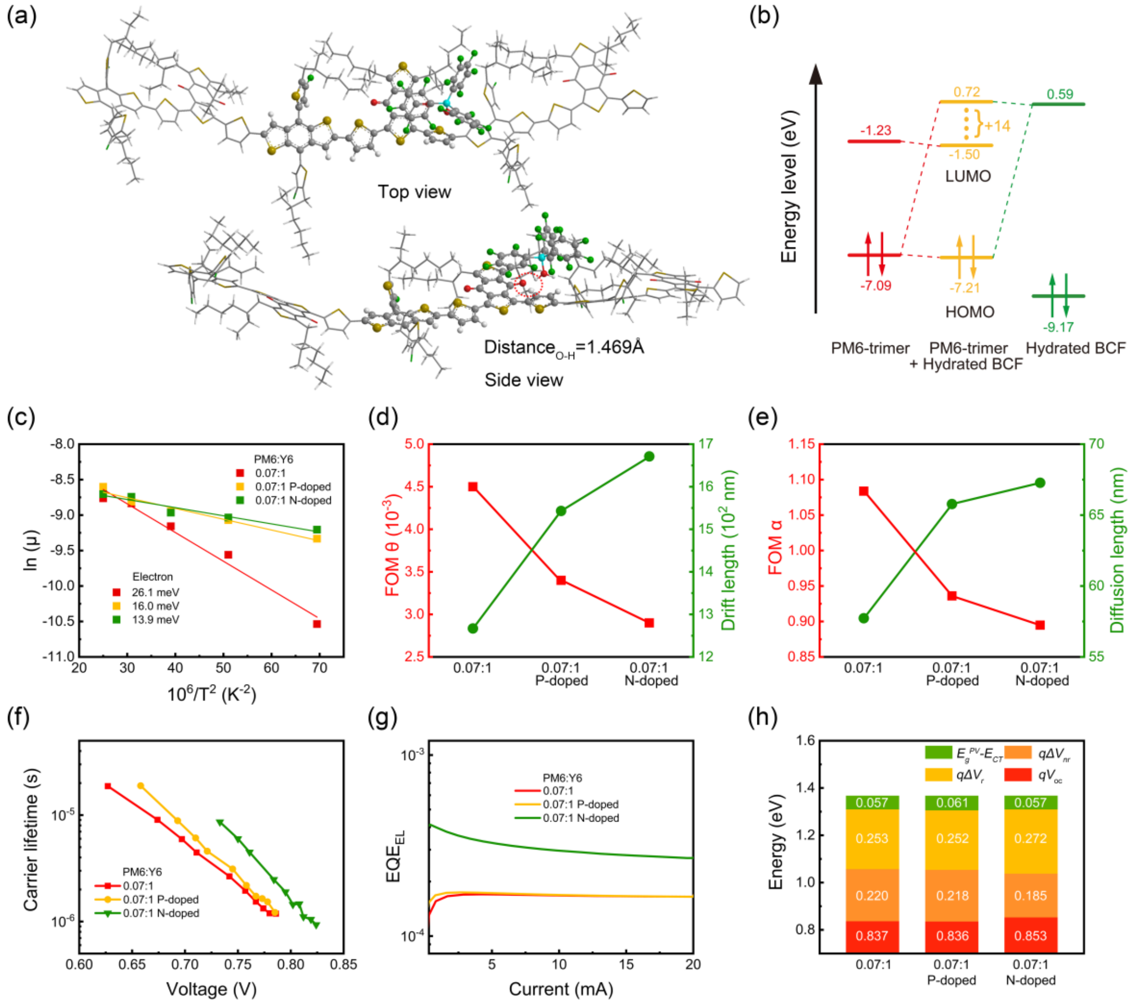

Figure 3. (a) Illustration of the molecular conformation of hydrated BCF doped PM6-trimer via DFT calculation. (b) Energy levels of PM6-trimer, hydrated BCF doped PM6-trimer, and hydrated BCF via DFT calculation. (c) Zero-field electron mobility versus the square of reciprocal temperature for the control, 0.5 wt% hydrated BCF doped, and 0.1 wt% N-DMBI doped PM6:Y6 (0.07:1) devices. (d) Values of $FoM\ \theta$ and l_{dr} for the control, 0.5 wt% hydrated BCF doped, and 0.1 wt% N-DMBI doped PM6:Y6 (0.07:1) devices. (e) Values of $FoM\ \alpha$ and l_{dif} for the control, 0.5 wt% hydrated BCF doped, and 0.1 wt% N-DMBI doped PM6:Y6 (0.07:1) devices. (f) TPV determined carrier lifetimes for the control, 0.5 wt% hydrated BCF doped, and 0.1 wt% N-DMBI doped PM6:Y6 (0.07:1) devices. (g) EQE_{EL} measurements for the control, 0.5 wt% hydrated BCF doped, and 0.1 wt% N-DMBI doped PM6:Y6 (0.07:1) devices. (h) Histograms of the energy loss for the control, 0.5 wt% hydrated BCF doped, and 0.1 wt% N-DMBI doped PM6:Y6 (0.07:1) devices. E_g^{PV}-E_{CT} is the charge generation energy loss, $q\Delta V_r$ is the radiative recombination energy loss, and $q\Delta V_{nr}$ is the nonradiative recombination energy loss.

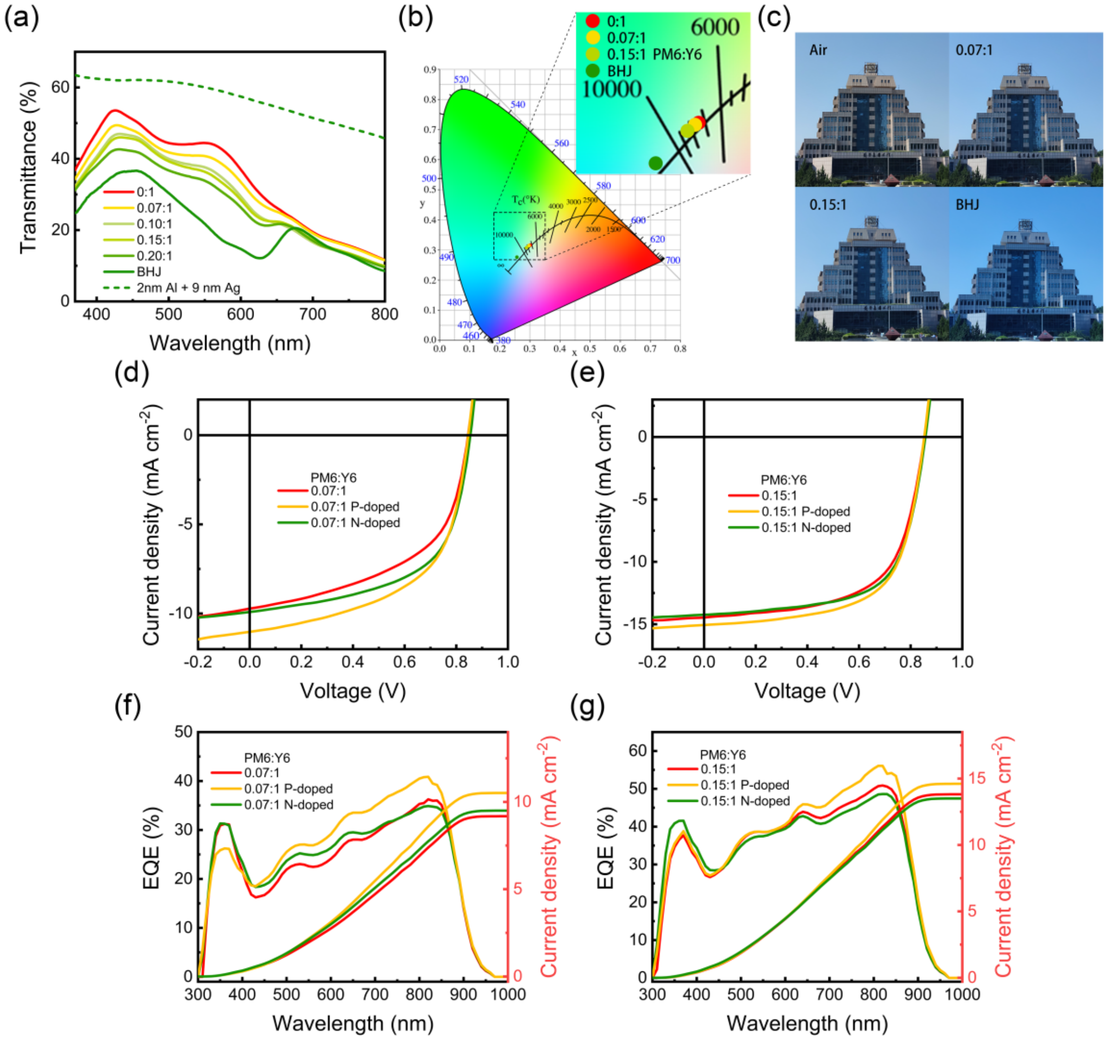

Figure 4. (a) The transmittance spectra of semi-transparent devices with various PM6:Y6 weight ratios (0:1, 0.07:1, 0.10:1, 0.15:1, 0.20:1, 0.83:1). (b) The color coordinates of devices with various PM6:Y6 weight ratios (0:1, 0.07:1, 0.15:1, 0.83:1). (c) Photographs of Qian Xuesen Library filtered by devices with various PM6:Y6 weight ratios (0:0, 0.07:1, 0.15:1, 0.83:1). (d-e) The *J-V* curves of the control, 0.5 wt% hydrated BCF doped, and 0.1 wt% N-DMBI doped semi-transparent PM6:Y6 (0.07:1) and (0.15:1) devices, respectively. (f-g) The *EQE* and corresponding integrated current density curves of the control, 0.5 wt% hydrated BCF doped, and 0.1 wt% N-DMBI doped semi-transparent PM6:Y6 (0.07:1) and (0.15:1) devices, respectively.

Table 1. Photovoltaic performance of the control, 0.5 wt% hydrated BCF doped, and 0.1 wt% N-DMBI doped opaque PM6:Y6 (0.07:1) devices.[a]

Materials	$V_{oc\ max}$ (V)	$V_{oc\ avg}$ (V)	FF_{max} (%)	FF_{avg} (%)	$J_{sc\ max}$ (mA cm^{-2})	$J_{sc\ avg}$ (mA cm^{-2})	PCE_{max} (%)	PCE_{avg} (%)	EQE (mA cm^{-2})
Control	0.84	0.84±0.01	52.3	52.2±0.6	17.2	17.1±0.2	7.6	7.5±0.1	17.2
P-doped	0.84	0.84±0.00	54.4	53.7±0.9	18.4	18.1±0.3	8.4	8.1±0.1	18.1
N-doped	0.85	0.85±0.01	57.6	55.8±1.0	17.2	17.3±0.3	8.5	8.2±0.1	17.3

[a] The maximum and average values were obtained from more than 15 independent devices.

Table 2. Photovoltaic performance of the control, 0.5 wt% hydrated BCF doped, and 0.1 wt% N-DMBI doped semi-transparent PM6:Y6 (0.07:1) and (0.15:1) devices.[a]

Materials		$V_{oc\ max}$ (V)	FF_{max} (%)	$J_{sc\ max}$ (mA cm^{-2})	$J_{sc\ avg}$ (mA cm^{-2})	PCE_{max} (%)	PCE_{avg} (%)	EQE (mA cm^{-2})	LUE (%)
0.07:1	Control	0.85	52.4	9.5	9.3±0.3	4.2	4.1±0.1	9.2	1.61
	P-doped	0.85	55.7	11.0	10.6±0.2	5.2	5.0±0.1	10.5	1.99
	N-doped	0.86	59.9	9.6	9.5±0.3	5.0	4.7±0.2	9.5	1.89
0.15:1	Control	0.85	62.3	14.5	14.2±0.2	7.7	7.5±0.1	13.8	2.61
	P-doped	0.85	64.2	15.1	14.6±0.3	8.3	7.9±0.1	14.6	2.80
	N-doped	0.86	65.3	14.3	14.1±0.2	8.0	7.8±0.1	13.5	2.72

[a] The maximum and average values were obtained from more than 15 independent devices.

Varying the blend ratio is effective to tune the optical properties of BHJ film for future application in semi-transparent and colorful power window. We discover that either type of molecular doping helps overcome the discontinuous charge transport networks led carrier recombination in dilute BHJ film. Our discovery provides a new methodology to reduce the electrical-optical gap of semi-transparent OSCs.

Y. Tang, H. Zheng,* X. Zhou, Z. Tang, W. Ma, H. Yan*

Molecular Doping Increases the Semi-Transparent Photovoltaic Performance of Dilute Bulk Heterojunction Film with Discontinuous Polymer Donor Networks